

Comparative analysis of in-situ and ex-situ synthesis of coconut husk cellulose nanofiber/copper-based metal-organic frameworks for curcumin uptake and release

Marvel Guntur Wijanarko^{a,b}, Maria Yuliana^{a,b,c,*}, Christian Julius Wijaya^{a,c},
Suryadi Ismadji^{a,c,*}, Michael Giovanni Sugiarto^a, Grandprix Thomryes Marth Kadja^{d,e,f},
Hidayat^{c,g}, Shella Permatasari Santoso^{a,b,c}, Wenny Irawaty^{a,c}, Sandy Budi Hartono^{a,c},
Felycia Edi Soetaredjo^{a,c}, Phuong Lan Tran-Nguyen^h

^a Department of Chemical Engineering, Widya Mandala Surabaya Catholic University, Kalijudan 37, Surabaya 60114, Indonesia

^b Chemical Engineering Master Program, Widya Mandala Surabaya Catholic University, Kalijudan 37, Surabaya 60114, Indonesia

^c Collaborative Research Center for Zero Waste and Sustainability, Kalijudan 37, Surabaya 60114, Indonesia

^d Division of Inorganic and Physical Chemistry, Faculty of Mathematics and Natural Sciences, Institut Teknologi Bandung, Ganesha 10, Bandung 40132, Indonesia

^e Center for Catalysis and Reaction Engineering, Institut Teknologi Bandung, Ganesha 10, Bandung 40132, Indonesia

^f Research Center for Nanosciences and Nanotechnology, Institut Teknologi Bandung, Ganesha 10, Bandung 40132, Indonesia

^g Research Center for Environmental and Clean Technology, National Research and Innovation Agency, Kawasan Puspiptek Gedung 820, Tangerang Selatan 15314, Indonesia

^h Faculty of Mechanical Engineering, Can Tho University, Can Tho, Vietnam

ARTICLE INFO

Keywords:

Coconut husk waste
Drug carriers
Cellulose nanofiber/Cu-BTC composite
Comparative study
Curcumin uptake/release
Sustainability

ABSTRACT

As a prominent global producer of coconut (*Cocos nucifera* L.), Indonesia yields an annual output above 6 million tons of coconut husk waste (CHW). This research uses CHW to fabricate the cellulose nanofibers (CNF) / copper-1,3,5-benzene tricarboxylate (Cu-BTC) composite to address the generated environmental issue using in-situ and ex-situ synthesis. The impact of different synthesis methods on composite properties and curcumin uptake/release performance is examined. The isolated CNF exhibits a fibrous morphology with a *ca.* 10 – 100 nm diameter, while the Cu-BTC particles are cubical with a side length of 4.1 μm . All CNF/Cu-BTC composites, resulting from the in-situ synthesis (C1) and ex-situ synthesis (with the crosslinkers of (1) triethylamine (C2); (2) citric acid (C3); (3) glutaraldehyde (C4)), display a flower branch-like topography, with Cu-BTC surrounding the CNF matrix. The C1 shows better dispersity of Cu-BTC on the CNF surface, while the two seem to aggregate in C2, C3 and C4. The curcumin uptakes of CNF, Cu-BTC, C1, C2, C3, and C4 are observed at 40.77 mg/g, 150.67 mg/g, 386.03 mg/g, 688.71 mg/g, 347.35 mg/g, and 294.84 mg/g, respectively. Among the composites, C2 exhibits higher uptake capabilities. This is due to the presence of triethylamine as an organic linker in C2, which provides more binding sites. Compared with the single component (CNF and Cu-BTC), the enhanced curcumin uptake of composites is credited to their three-dimensional interior structure, which increases the number of binding sites. The uptake performance of all composites follows a modified pseudo-first-order law and multilayer mechanism. The curcumin and composite interactions are driven by Van Der Waals interaction, hydrogen bonding for the first layer, and ion exchange for the upper layers. The release study of curcumin from composites shows slow release, and C2 has the highest release, with 36.7 % at pH 7.4 and 39.1 % at pH 5.5.

1. Introduction

A drug delivery system (DDS) is defined as a controlled system and a formulation enabling the introduction of medicinal products into the

body. Studies show that DDS can improve outcomes in many ways, including enhanced therapeutic efficacy, reduced toxicity, increased patient compliance, enabling entirely new medical treatments, and controlling the rate, time, and target release (Adeosun et al., 2020; Gao

* Corresponding authors at: Department of Chemical Engineering, Widya Mandala Surabaya Catholic University, Kalijudan 37, Surabaya 60114, Indonesia.

E-mail addresses: mariayuliana@ukwms.ac.id (M. Yuliana), suryadiismadji@yahoo.com (S. Ismadji).

<https://doi.org/10.1016/j.indcrop.2024.120048>

Received 28 July 2024; Received in revised form 23 October 2024; Accepted 9 November 2024

Available online 19 November 2024

0926-6690/© 2024 Elsevier B.V. All rights reserved, including those for text and data mining, AI training, and similar technologies.

et al., 2023; Mallakpour et al., 2022). The critical characteristics in designing drug carriers are their biocompatibility, high loading capacity, and controlled release (Mallakpour et al., 2022). However, research has recently pointed out that drug carriers with additional features, e.g., nano-size and good antimicrobial performance, are preferable, as the two give a combined function of the improved delivery system and antimicrobial activity (Mallakpour et al., 2022).

Metal-organic frameworks (MOFs) are porous and nano-sized materials that have various active sites and exceptional characteristics, e.g., chemically and thermally stable, wide surface area, tunable pore size, and facile surface modification, making them ideal candidates for drug carrier (Li et al., 2023; Tu et al., 2022; Zhao et al., 2019). They are well-known for their tunability and versatility to be composited with other materials as previously studied, e.g., MIL-53-NH₂@natural fabric to remove liquid-fuel nitrogenated contaminants (Abdelhameed et al., 2018), Zn-MOF@cellulosic fiber for selective separation of chlorophyll (Emam et al., 2023), mesoporous composite of microcrystalline cellulose and zeolitic imidazole frameworks for temperature-controlled-release of essential oil (Abdelhameed et al., 2021), IRMOF-3/MIL-68-NH₂/cotton for fuel purification (Emam et al., 2022), Cu-BTC@natural fabrics for the release of insect repellent (Emam and Abdelhameed, 2017), and cellulose microfiber@ZIF-8 composite for curcumin delivery (Wijanarko et al., 2023). Several metal ions synthesizing MOFs, e.g., Ag⁺, Fe³⁺, Zn²⁺, and Cu²⁺, are essential in inducing antimicrobial activities (Li et al., 2023). Cu-BTC was selected for this research due to the presence of coordinatively unsaturated metal sites (Cus) with antibacterial properties. Copper is also known to have lower toxicity than other metals. The study conducted by Liang et al. (2022), which investigates the potential use of curcumin-loaded Cu-BTC/carboxymethyl starch-based composite for food preservation, reported that Cu-BTC acts as a curcumin carrier and forms synergistic antibacterial with curcumin, which indicates its potential as the application of a drug (Li et al., 2023; Liang et al., 2022). Moreover, Cu-BTC can control drug release, as Chen et al. (2017) reported (Chen et al., 2017). However, Cu-BTC has drawbacks such as instability in water and ease of aggregate, which are fundamental flaws that pose significant challenges to its utilization in drug delivery (Tu et al., 2022; Zhang et al., 2021).

To mitigate the drawbacks, biocompatible cellulose, in the form of cellulose nanofiber (CNF) or cellulose nanocrystal (CNC), is an ideal candidate to be combined with Cu-BTC because of its active group of polymers (Huo et al., 2022; Zhang et al., 2021). The CNF gives more advantages than CNC because it provides a larger specific area, better mechanical stability, stronger tensile strength, and surface charge density; moreover, the carboxylate content in CNF increases the adsorption ratio (Isogai et al., 2011). Besides, for long-term drug storage, the CNF's nanofiber–nanofiber interaction and high crystallinity give oxygen-sensitive drugs oxidative stability, providing oxygen barrier properties at low humidity. Due to its distinctive 3D nanofibrous network structure, the unique characteristics of CNF, including hydrophilicity, biodegradability, non-toxicity, pH sensitivity, high modulus, and tensile strength, may promote cell penetration and proliferation. However, CNF alone has poor drug release in drug delivery applications, as reported by several studies (Kolakovic et al., 2013, 2012; Löbmann et al., 2017; Svagan et al., 2017). Therefore, combining CNF and Cu-BTC may improve the drug uptake/release performance (Sarkar et al., 2017).

Generally, cellulose and MOF composite can be fabricated using the in-situ and ex-situ growth methods. Among the three popular types of in-situ growth techniques (one-pot, step-wise, and layer-by-layer methods), the step-wise synthesis method is suitable for in-situ growth of CNF/Cu-BTC because Cu-BTC growth on CNF is heavily affected by the order of mixing procedures (da Silva Pinto et al., 2012). Some advantages of in-situ synthesis are as follows: (1) the distribution and uniformity of MOF on the surface of CNF are easily optimized, and (2) a higher MOF load can be achieved due to the presence of multiple crystallization nucleation sites, which allows adequate interaction between cellulose fibers and MOFs (Zhang et al., 2021).

Meanwhile, the ex-situ growth process implies that MOF crystals are formed before the fabrication of the composite (Tu et al., 2022). This research uses the direct mixing technique, adding organic crosslinkers to bridge the interaction between Cu-BTC and CNF (Abdelhameed et al., 2016). Compared with the in-situ synthesis, ex-situ synthesis has defects – MOF tends to agglomerate during the process, which is unavoidable, and the affinity between MOF and cellulose is weak. Despite its drawbacks, the advantage of using ex-situ synthesis is controllable MOF loading. In addition, the ex-situ technique helps CNF avoid harsh MOF synthesis conditions during composite formation (Tu et al., 2022; Zhang et al., 2021). In typical ex-situ synthesis, to improve the binding between CNF and MOF, the crosslinking agent addition might help to enhance its uptake and release capabilities. Triethylamine (TEA), citric acid, and glutaraldehyde are chosen for comparison studies based on their overall charges and affinity.

In this study, coconut (*Cocos nucifera* L.) husk waste (CHW), a significant solid waste in Indonesia, is selected as the cellulose source due to its high content of α -cellulose (26.6 %) (Sangian and Widjaja, 2018). Using CHW may be an opportunity to reduce the masses of solid waste and, at the same time, to increase its economic value. This work employs chemical oxidation using 2,2,6,6-tetramethylpiperidinyloxy (TEMPO) to reduce the size of the cellulose into CNF. Introducing TEMPO helps to oxidize the hydroxyl groups in anhydroglucose units to a carboxyl group and create repulsion in each fiber (Shih et al., 2020). Therefore, the TEMPO-oxidized cellulose gives well-separated nanofibers and is decorated with the carboxylate groups, which enables interaction with the positive charge of metal and strengthens the metal binding, hence increasing the chance of Cu-BTC to be attached to CNF (Isogai et al., 2011; Zhu et al., 2020). With the complementary properties of CNF and Cu-BTC, this research studies (1) the characterization of CNF/Cu-BTC composites obtained from the in-situ and ex-situ methods, (2) their performances on the curcumin uptake, and (3) the release behavior of the composites obtained from the in-situ and ex-situ syntheses.

2. Research methodology

2.1. Materials

The CHW is obtained from a local supplier in Bandung, Indonesia, while curcumin is purchased from PT. Javaplant Indonesia. All reagents are procured from Merck (Germany) and are of analytical grade; therefore, they are used without further purification.

2.2. Preparation of CHW-based CNF

Initially, CHW is dispersed in a two percent NaOH solution for two hours at 100°C to remove impurities and waxy materials covering the surface of fiber cell walls (Dinand et al., 1996), then washed and filtered. The cleansed CHW is subjected to an alkali pretreatment (with the mass ratio of NaOH solution (20 %) to fiber = 30:1) for two hours and decanted to separate fibers from the supernatant. The procedure is repeated twice to obtain the delignified fibers (DF). DF is then hydrolyzed using NaClO solution (12 %, 100 mL) and acetic acid (99 %, 12 mL) for two hours at 100°C. About 200 mL of cold water is added to the solution to stop the reaction. The suspension is subsequently filtered to separate the solid from the supernatant. The hydrolysis process is repeated two times before being water-washed until the pH reaches 7.0 and oven-dried for 12 h to obtain hydrolyzed cellulose (HC).

In the typical synthesis of CNF, 1 g of HC is initially dispersed in a phosphate buffer saline (PBS) solution (90 mL, pH = 6.8). Then, about 1.13 g of NaClO₂ and 0.016 g of TEMPO are added to the HC-PBS mixture. A 0.1 M NaClO solution is prepared in a separate system by diluting 12 % NaClO using PBS (pH = 6.8) solution as a solvent. Subsequently, 0.5 mL of the prepared NaClO solution is added to the HC-PBS mixture to initiate the TEMPO oxidation. The system is then stirred and sonicated simultaneously for four hours at 60 °C. Once the reaction

completes, the system is cooled down to room temperature and water-washed two times. This procedure is repeated twice to obtain TEMPO-oxidized CNF, hereafter referred to as CNF.

2.3. Synthesis of CNF/Cu-BTC Composite

The in-situ synthesis of CNF/Cu-BTC composite occurs at room temperature and follows the procedure proposed by Hao et al. (2022) (Hao et al., 2022) with slight modification. Initially, 2.42 g of Cu (NO₃)₂·3H₂O are dissolved in 30 mL water and stirred for 30 min (Solution A). Then, 0.17 g of CNF is added to solution A and mixed for 24 h. The ligand solution (solution B) is prepared by dissolving H₃BTC (2.1 g) in 15 mL DMF and 15 mL ethanol with continuous stirring for 15 min. The two solutions are mixed and homogeneously agitated at constant rotational speed (600 rpm) for 30 h. The resulting solid is sequentially washed with DMF and methanol twice (so-called methanol exchange) and dried using a vacuum oven at 200 mbar and 60°C; the resulting product is denoted as C1.

The ex-situ synthesis of the CNF/Cu-BTC composite follows similar procedures as in the in-situ synthesis; however, without adding CNF to solution A. Consecutively, solution B is added dropwise to solution A, stirred for 30 h, washed using dimethylformamide and ethanol twice, and vacuum dried (200 mbar, 60°C). The newly formed Cu-BTC particles are subsequently mixed with the CNF solution (1 g CNF in 120 mL water), during which 6 mL of crosslinkers is added dropwise while stirring for two hours. Several crosslinkers are used in this experiment, e. g., TEA, citric acid, and glutaraldehyde – whose composite products will be denoted as C2, C3, and C4, respectively. The resulting solid cake is collected by centrifugation, washed repeatedly using DMF, activated via methanol exchange, and vacuum dried (200 mbar and 60°C) to obtain C2, C3, and C4 powders.

2.4. Characterization of CNF, Cu-BTC, and CNF/Cu-BTC composites (C1, C2, C3, and C4)

The surface morphologies of CNF, Cu-BTC, C1, C2, C3, and C4 are characterized using scanning electron microscopy (SEM) (JEOL JSM-6500F, Jeol, Ltd., Japan) at an accelerating voltage of 5 – 10 kV. The elemental mapping of C1 – C4 is conducted using the EDX feature in the SEM instrument. Meanwhile, the transmission electron microscopy (TEM) images of C1 – C4 are taken using Hitachi HT7700 (Hitachi, Ltd., Japan) at 120 kV. The X-ray Powder Diffraction (XRD) analysis (X'PERT Panalytical Pro X-ray diffractometer, Philips-FEI, Netherlands) at 2θ = 5 – 60°, tube current = 40 mA, running voltage = 40 kV, and constant Cu K_{α1} radiation, λ = 1.542 Å is carried out to determine the crystal structure of CNF, Cu-BTC, C1, C2, C3, and C4. The FTIR spectra are acquired using Shimadzu FTIR 8400 s from 400 to 4000 cm⁻¹. The textural properties of CNF, Cu-BTC, C1, C2, C3, and C4 are measured using a Micromeritics ASAP 2010 sorption analyzer (Micromeritics Instrument Corporation, USA) at 77 K after degassing the sample for two hours at 423 K. Last, the surface charge of all samples is determined by pH_{pzc} analysis using the drift method.

2.5. Curcumin uptake

The uptake study of curcumin to CNF, Cu-BTC, C1, C2, C3, and C4 composites compares their performance and, at the same time, determines the suitable synthesis technique of the CNF/Cu-BTC composite. All experimental runs start by adding 0.4 % (w/v) carrier to a 100 mL-ethanolic curcumin solution (1000 mg/L). The mixture is then agitated at room temperature for 24 h. After the adsorption completes, the supernatant is collected and analyzed using a spectrophotometer UV-Vis 2600 (Shimadzu, Japan) at λ = 429 nm to determine the loaded curcumin (Q, mg/g) in all samples. Further, the statistical t-test using a 95 % confidence level is employed to determine whether the uptake capacity among all materials is statistically significant.

The uptake capacity at a specific time (Q_t) and equilibrium (Q_e) are computed using the following equations to study the behavior of the curcumin loading, where C₀, C_t, and C_e respectively represent the curcumin concentration at t = 0, t = t, and t = t_{eq} (mg/L), m_c corresponds to the loaded mass of solid (g), and V equals to the volume of curcumin solution. The temperature is maintained at three levels (T = 30, 40, 50°C).

$$Q_t = \frac{(C_0 - C_t)V}{m_c} \quad (1)$$

$$Q_e = \frac{(C_0 - C_e)V}{m_c} \quad (2)$$

All the data are then fitted to several kinetic (pseudo-first-order (PFO), pseudo-second-order (PSO), Elovich, modified PFO, modified PSO, mixed pseudo order (MPO), and pseudo-n-th order (PNO)) and isotherm (Langmuir, Freundlich, Temkin, Dubinin-Radushkevich (D-R), Brunauer-Emmett-Teller (BET)) plots, as summarized in Table S1 and Table S2, to understand the uptake behavior. The obtained isotherm parameters are further analyzed to determine Gibbs free energy (ΔG°), enthalpy (ΔH°), and entropy (ΔS°).

2.6. Curcumin release

In the typical release method, the curcumin-loaded CNF/Cu-BTC (Cur@CNF/Cu-BTC) composites are immersed in pH-adjusted PBS solution for 96 h with varied sampling time intervals. Initially, 200 mg of Cur@CNF/Cu-BTC is introduced into a membrane containing 5 mL of phosphate buffer saline (PBS) ethanolic solution (with the volume ratio of ethanol: water = 7:3 (George et al., 2019)). Then, the membrane containing the particles is immersed in 500 mL of PBS solution while constantly stirred. The five-milliliter solution is withdrawn at various release intervals (10 min to 96 h). Subsequently, the solution taken during sampling is replaced with a fresh PBS solution to maintain constant release volume. The withdrawn samples are analyzed using Shimadzu UV-Vis spectrophotometer 2600 (Shimadzu, Japan) at λ = 429 nm. The release system is adjusted to pH = 5.5 and pH = 7.4 to mimic the blood plasma condition. The release behavior is studied using several kinetic models, including Higuchi, Hixson-Crowell, and Korsmeyer-Peppas, as summarized in Table S3.

3. Results and discussions

3.1. Characterization of CNF, Cu-BTC, and their composites

The CNF is successfully derived from CHW, with a substantial yield of 25.1 %. The cellulose content present in CNF is observed at 79.44 %, while the remaining are hemicellulose (7.70 %), hot water soluble (5.17 %), lignin (7.68 %), and ash (0.01 %). Fig. 1a presents the SEM image of CHW-based cellulose with a bulk fiber diameter of 9 μm. One cellulose fiber possesses a stacked and twisted rod configuration with an individual fiber diameter of ca. 10 – 100 nm. This finding suggests that a suitable treatment may disentangle the stacked and twisted structure, reducing the fiber size to the nanometer scale.

Fig. 1b–c shows the morphology images of CNF, which is derived from the cellulose through the TEMPO-oxidation procedure. The SEM image (Fig. 1b) reveals the mean diameter of CNF at ca. 20 nm (measured using ImageJ version 1.5k), confirming the presence of nanofibers. Further, the TEM analysis (Fig. 1c) supports the existence of nanometer-size fibrous structures within the examined sample; the diameter of the fiber is found at ca. 8 nm. Meanwhile, Fig. 1d–f corresponds to the morphological shape of Cu-BTC after the methanol exchange, which is cubical. Before the methanol exchange (Figure S1), the irregular surface of Cu-BTC particles exhibits the presence of impurities surrounding the primary object, hindering the visibility of its cubical forms. Particle aggregation is also detected, which could worsen the

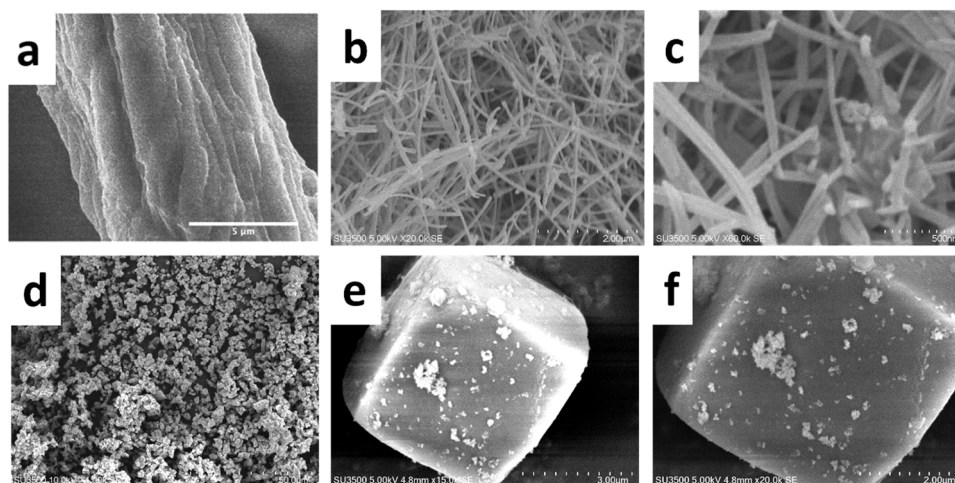


Fig. 1. Morphological structures of (a) cellulose, (b–c) CNF, and (d–f) Cu-BTC.

textural properties of Cu-BTC. In contrast, the SEM image of Cu-BTC after methanol exchange demonstrates a cubical structure characterized by a side length of 4.1 μm . The development of a cubical shape arises from the coordination bonds between particles. Feng et al. (2019) discuss the influence of the copper precursor on Cu-BTC morphology in their review paper (Feng et al., 2019). Applying preformed copper paddlewheel secondary building units, particularly copper acetate, as a metal source enhances growth along the (111) lattice plane, leading to the development of cubic morphologies (Diring et al., 2010; Umemura et al., 2011). Gautam et al. (2022) reported that Cu-BTC with cubical morphology exhibits a greater surface area than the commonly found octahedral form (Gautam et al., 2022).

The morphology images of C1 to C4 are presented in Fig. 2a–c, Fig. 2g–i, Fig. 2m–o, and Fig. 2s–u, revealing a flower branch-like morphology in which a CNF matrix surrounds the Cu-BTC particles. While C1 shows a greater dispersity in the distribution of Cu-BTC particles on the surface of CNF, the other three composites (C2, C3, and C4) seem to have their cellulose and Cu-BTC agglomerate with each other (seen in Fig. 2g–i, Fig. 2m–o, Fig. 2s–u). It supports the theory that the uniformity of the composite can be easily achieved in the in-situ

synthesis. The elemental mappings of C1 to C4 (Fig. 2d–f, Fig. 2j–l, Fig. 2p–r, and Fig. 2v–x) present that in-situ and ex-situ composites exhibit a high presence of Cu-BTC, as indicated by the signal detection of copper clusters. However, a stronger signal of copper is monitored in ex-situ synthesis (Fig. 2l, Fig. 2r, and Fig. 2x) than in in-situ synthesis (Fig. 2f), indicating that a higher amount of Cu-BTC is attached to the surface of CNF. The high intensity of carbon and oxygen signals in all ex-situ syntheses (Fig. 2j–k, Fig. 2p–q, Fig. 2v–w), compared with that in in-situ, implies that both Cu-BTC and cellulose matrix are equally dominant on the surface of ex-situ – proving the ability of the ex-situ synthesis to control the proportion of MOF during the synthesis. However, fewer copper clusters were detected in C3 among the ex-situ synthesized composites. Given that the overall charge of citric acid is neutral compared with CNF, the attachment of this crosslinker to the fibrous matrix is less sturdy, resulting in less Cu-BTC attached on the surface of the CNF (He et al., 2021; Mali et al., 2018; Mikušová and Mikuš, 2021).

The presence of cellulose matrix on the surface of C2 is also supported by the XRD spectra (Fig. 3), where a cellulose hump ($2\theta = 22.4^\circ$) is seen in C2. Meanwhile, the non-appearance of cellulose diffraction peaks in C1, C3, and C4 can be attributed to the Cu-BTC formation in

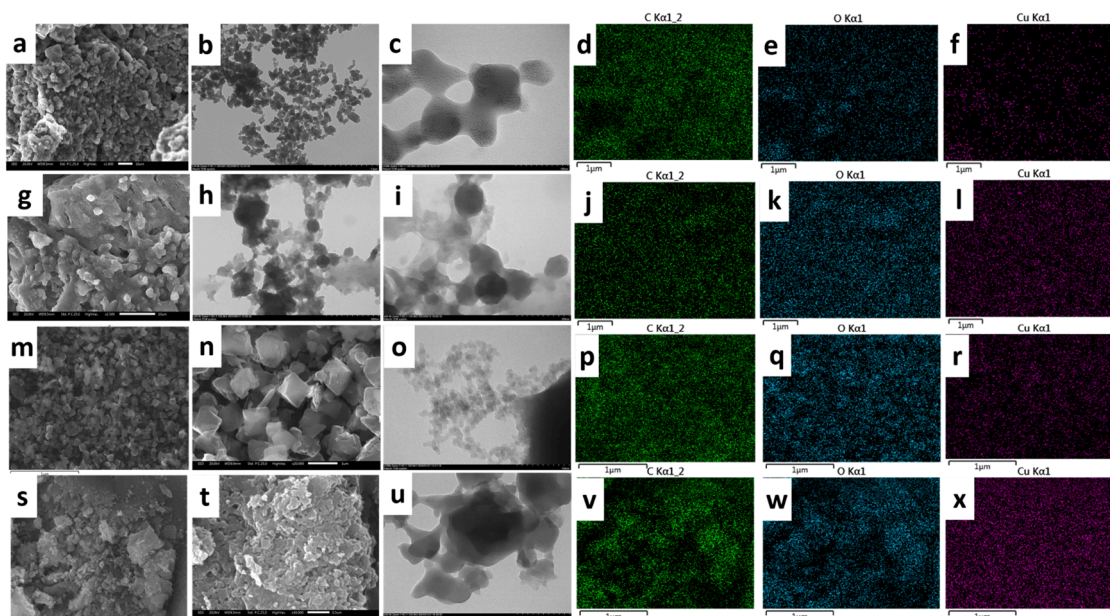


Fig. 2. Various surface characterizations of (a–f) C1, (g–l) C2, (m–r) C3, and (s–x) C4.

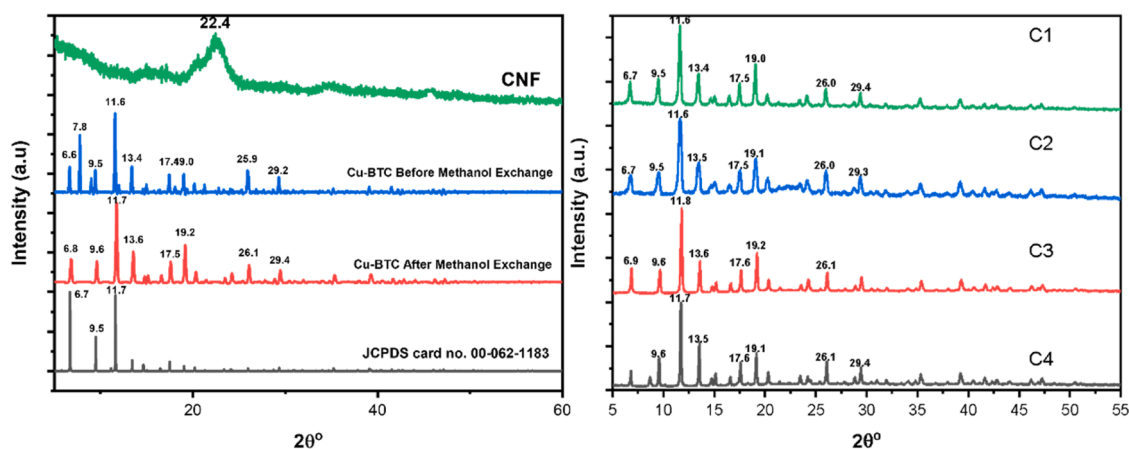


Fig. 3. The diffraction spectra of CHW-based CNF, Cu-BTC before- and after methanol exchange, C1, C2, C3, and C4.

conjunction with cellulose, possibly covering the whole surface of cellulose with Cu-BTC.

Fig. 3 also shows eight strong diffraction peaks for both Cu-BTC particles before- and after methanol exchange at $2\theta = 6.9^\circ$, 9.7° , 11.8° , 13.5° , 17.5° , 19.2° , 26.1° , and 29.5° , which correspond to the lattice planes 200, 220, 222, 400, 511, 440, 731, and 110, respectively (Chen et al., 2018; Gautam et al., 2022). The crystal structure of the synthesized Cu-BTC is consistent with the simulated Cu-BTC, indicating a successful synthesis using the current method. A significant peak intensity at $2\theta = 7.8^\circ$ observed in Cu-BTC before methanol exchange potentially indicates the presence of unreacted copper metal precursor trapped within Cu-BTC (Chen et al., 2018). The absence of this peak after the solvent exchange implies a successful removal of impurities from Cu-BTC particles. Three fingerprint peaks of Cu-BTC at $2\theta = 6.7^\circ$, 9.5° , and 11.6° are all observed in C1, C2, C3, and C4, implying the successful impregnation of Cu-BTC on the surface of the composites. The peak consistency with the XRD analysis of a single Cu-BTC denotes no significant change in the morphology of Cu-BTC crystals attached to the composites. A crystallinity degree of 51.6% is achieved for the CNF solid.

Fig. 4 summarizes the FTIR analysis of the single materials (CNF and Cu-BTC) and their composites (C1 – C4). The CNF exhibits distinct peaks in the FTIR analysis within the range of $3500\text{--}3300\text{ cm}^{-1}$, 2895 cm^{-1} , 1633 cm^{-1} , and 1078 cm^{-1} . The broad peak at $3500\text{--}3300\text{ cm}^{-1}$ corresponds to the strong hydrogen bonding (O-H) in the CNF matrix, meso

Cu-BTC, and adsorbed water. As CNF and Cu-BTC surfaces possess many O-H groups, combining the two materials via in-situ synthesis (C1) increases the peak transmittance of the hydrogen bonding. In contrast, the reduced peak transmittance at $3500\text{--}3300\text{ cm}^{-1}$ is observed for C2 – C4, which is likely because the crosslinkers used during the ex-situ synthesis may replace the O-H group in CNF and Cu-BTC. The C-H stretching vibration of the methyl and methylene groups is observed at 2895 cm^{-1} . The peak at 1633 cm^{-1} is associated with the O-H bending of adsorbed water in the matrix and a double bond between carbon and oxygen ($\text{C}=\text{O}$). Finally, the peak at 1078 cm^{-1} signifies the carbon bonding with oxygen (C-O) (Setyaningsih et al., 2018). The FTIR analysis of Cu-BTC indicates the presence of specific peaks at 732 cm^{-1} , 1370 cm^{-1} , 1645 cm^{-1} , and 3450 cm^{-1} . These peaks correspond to the bending and stretching vibrational modes of Cu-O, the vibrations of the carboxylate group (C-O and $\text{C}=\text{O}$) to Cu ions, and the presence of surface-adsorbed water and OH group in Cu-BTC, respectively. The bending vibration of the aromatic ring induces small peaks at 660 and 732 cm^{-1} (Liu et al., 2022).

Meanwhile, similar profiles are observed throughout C1 to C4. The peak at $470\text{--}730\text{ cm}^{-1}$ denotes the presence of Cu-O, indicating that Cu-BTC particles are incorporated into the composites. Several other peaks are also detected in these composites: 1100 cm^{-1} (C-O), 1375 cm^{-1} (vibration of the carboxyl group with Cu ions), 1644 cm^{-1} (O-H bending; $\text{C}=\text{O}$), 2931 cm^{-1} (C-H stretching), and 3419 cm^{-1} (O-H), which are also present in both CNF and Cu-BTC. The analysis shows no

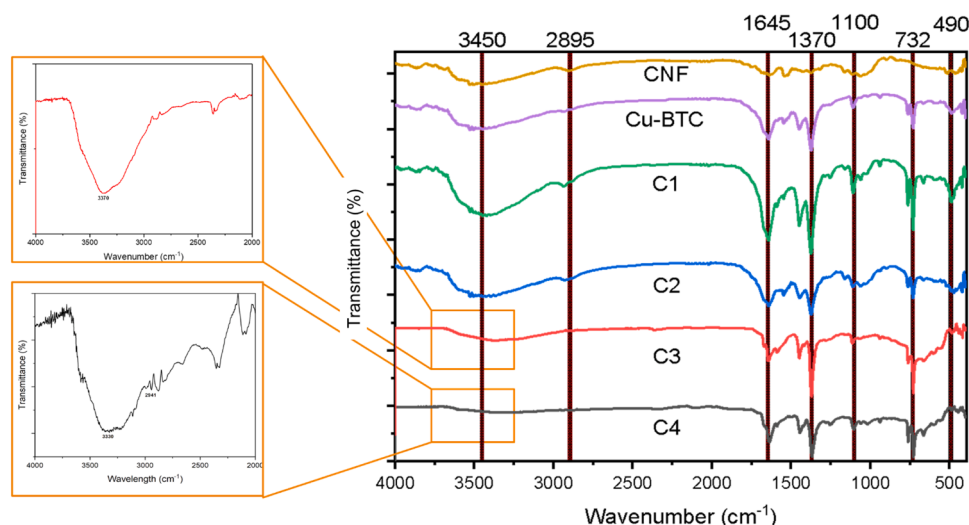


Fig. 4. The FTIR spectra of CHW-based CNF, Cu-BTC, C1, C2, C3, and C4.

significant changes in the functional group during the synthesis of C1 to C4.

The surface charges of all materials are measured using pH_{pzc} analysis, and the results are depicted in Fig. 5a–d. The pH_{pzc} of CNF intersects at $\text{pH} = 6.8$, while it is found at $\text{pH} = 4.4$ for Cu-BTC (Peedikakkal and Aljundi, 2020). These findings imply that both materials have a mild acidic character, with a positive charge below the intersection point and a negative charge above the intersection.

The intersection points for C1, C2, C3, and C4 are observed at $\text{pH} = 3.8, 2.8, 3.9,$ and 3.8 , respectively. Based on the experimental results, the neutral charge of CNF shifts from $\text{pH} = 6.77$ (neutral) to acidic when combined with Cu-BTC. This shift is attributed to positive ions in Cu-BTC (copper sites), indicating that Cu-BTC is the dominant factor even after being composited with CNF (Peedikakkal and Aljundi, 2020). The pH_{pzc} value of C2 is monitored to be lower than the others. The observed phenomenon may be credited to the alterations in the electrochemical properties of the material, mainly due to the existence of TEA as a crosslinker for C2. The present findings align with the results reported by Li et al. (2019), which demonstrate that modifying Cu-BTC with TEA leads to changes in its electrochemical properties (Li et al., 2019).

A visual inspection of both materials reveals that the C1 composite exhibits degradation during the pH_{pzc} analysis, characterized by the formation of black floc solid, within 24 h at $\text{pH} = 12$. Conversely, the C2, C3, and C4 composites reveal no degradation at similar conditions. This occurrence of the black solids might be due to the detachment of the BTC ligand from the copper metal, followed by the attachment of the metal to NaOH solution, which produces CuO (black floc solid). The results confirm the findings of Abdelhamid et al. (2022); this study highlights the use of metal in combination with free oxide to form ZnO before reconstructing itself to become ZIF-8 (Abdelhamid et al., 2022).

The N_2 adsorption-desorption profiles of CNF, Cu-BTC, C1, C2, C3, and C4 (Fig. 6) follow the isotherm profile type II, indicating microporous or non-porous material. The CNF exhibits non-porous and has no identifiable monolayer formation, while Cu-BTC, C1, C2, C3, and C4 are microporous. The type II isotherm is commonly associated with a

multilayer mechanism, indicating the possible existence of multilayer adsorption. This phenomenon is also verified by the steep increase in the adsorption profiles of all samples at $P/P_0 = 0 - 0.1$ and $0.8 - 1.0$. The first sharp increase between $P/P_0 = 0 - 0.1$ indicates that the adsorbed molecules start to fill the pores, while the P/P_0 values between $0.2 - 0.7$ exhibit a steady gradual increase – marking the completion of monolayer adsorption. The second sharp increase between $P/P_0 = 0.8 - 1.0$ indicates a significant amount of overlapped monolayer and the onset of multilayer adsorption (Thommes et al., 2015). An anomaly is seen in the CNF's desorption graph, which is lower than its adsorption counterpart – this may be attributed to some structure in CNF or impurities being vacuumed during the N_2 sorption analysis, resulting in the possible structure defect and loss of mass. The difference between adsorption and desorption is negligible for CNF, Cu-BTC, C1, and C4.

In contrast to the other three materials, C2 and C3 exhibit a bottle-neck form in the desorption graph, showing the H3 hysteresis loop. This hysteresis usually implies the plate-like particles with a grooved-pore network (Thommes et al., 2015; Yurdakal et al., 2019). The observed open-loop hysteresis of all samples, except Cu-BTC, is caused by the swelling of the polymer-polymer interaction. Since there is no thermodynamic explanation for the adsorbate to desorb at low relative pressure, the expansion of already-existing pores and the creation of new ones in the restricted-access (extremely narrow) openings will inversely cause the adsorbed component to be retained inside, resulting in incomplete desorption. The addition of hydrogen bonding caused by the interaction between the cellulose matrix and Cu-BTC makes it harder for the matrix to return to its original shape after desorption (Jeromenok and Weber, 2013; Weber et al., 2011).

The textural properties of all materials are summarized in Table 1. The composite of C2 indicates the highest textural properties, possibly caused by using TEA as crosslinkers. (Zhang and Pinna, 2024) reported that TEA may slowly deprotonate the ligand, opening more pores and giving CNF more access to interconnecting the ligand with the Cu-BTC. This phenomenon increases the pore diameter of C2, allowing higher capacity of curcumin loading.

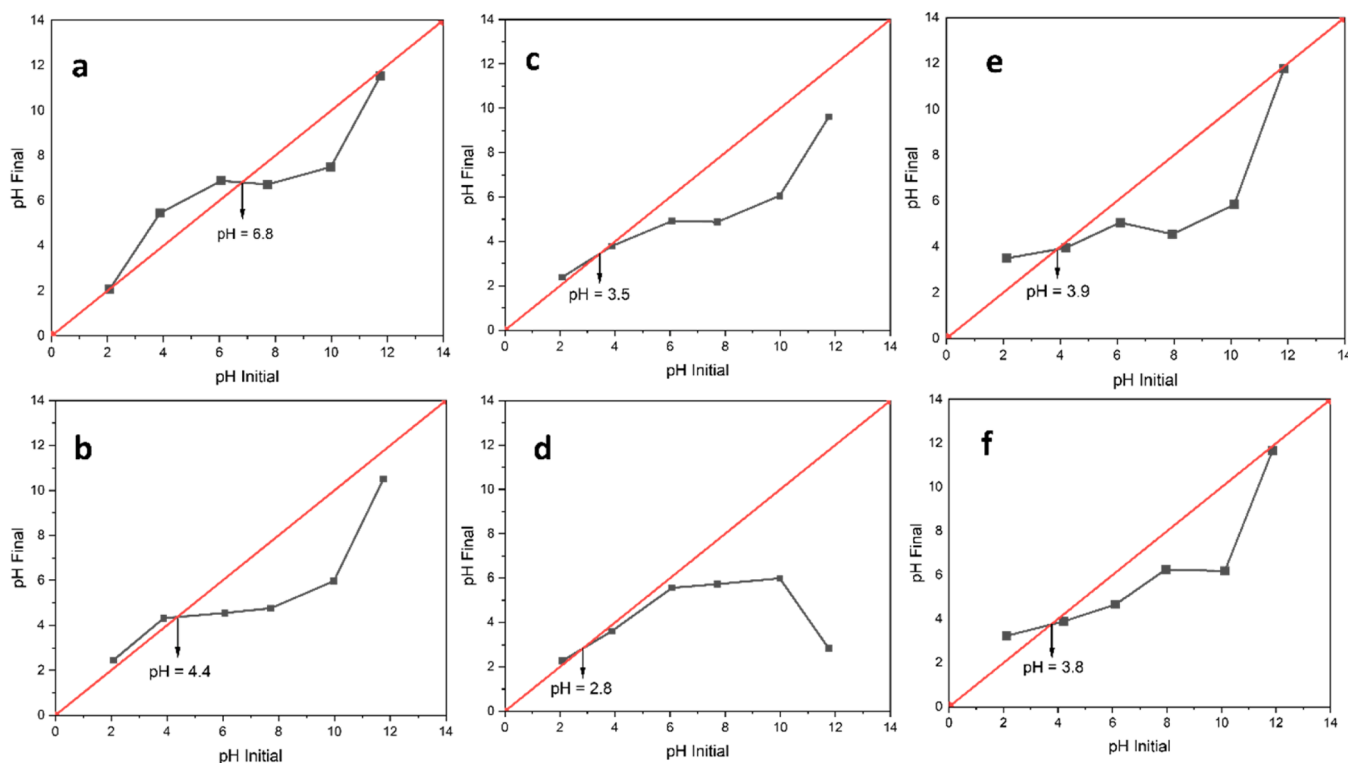


Fig. 5. The pH_{pzc} of (a) CNF, (b) Cu-BTC, (c) C1, (d) C2, (e) C3, and (f) C4.

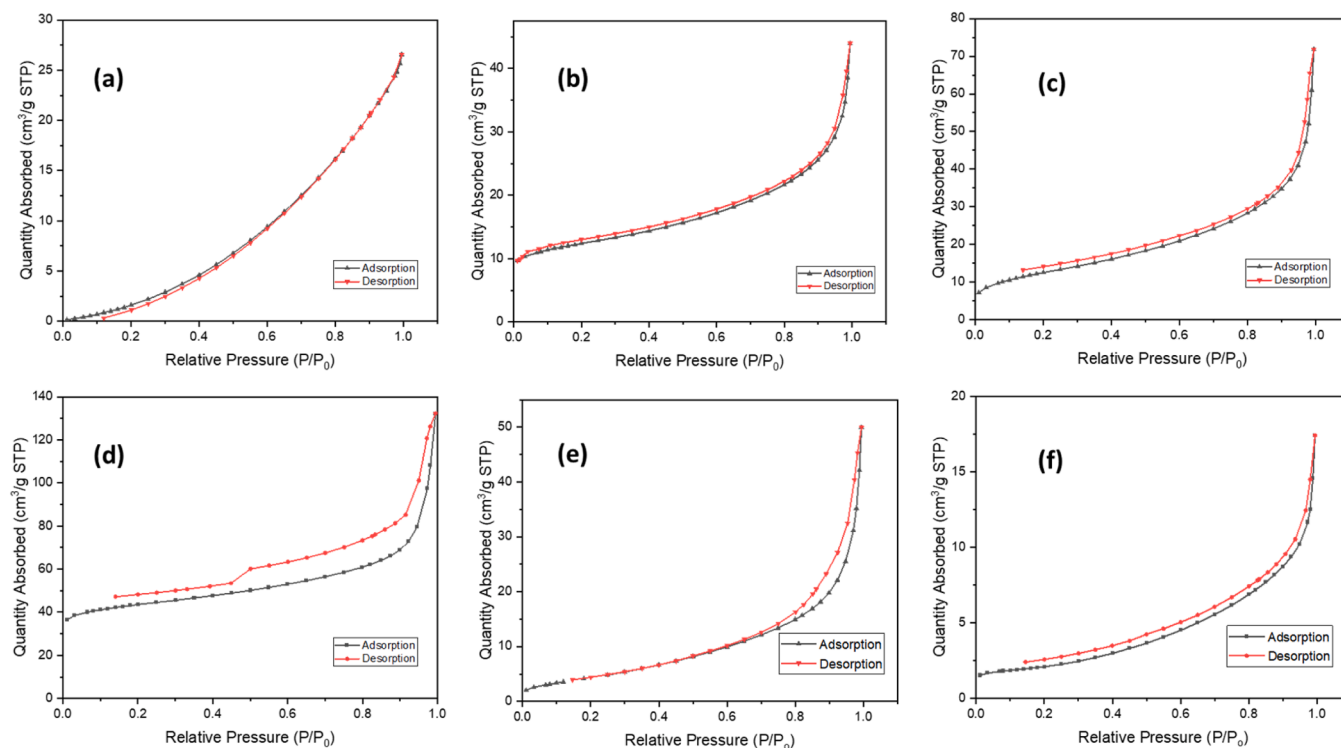


Fig. 6. The N_2 adsorption-desorption profiles of (a) CNF, (b) Cu-BTC, (c) C1, (d) C2, (e) C3, and (f) C4.

Table 1

The textural properties of CNF, Cu-BTC, C1, C2, C3, and C4.

Material ^a	Surface Area (m ² /g)	Pore diameter (nm)	Pore Width (nm)
CNF	36.7	4.2	6.6
Cu-BTC	41.9	5.2	10.6
C1	43.6	7.2	10.7
C2	143.3	46.2	13.3
C3	17.4	12.6	13.8
C4	7.4	10.5	11.7

^a C1: CNF/Cu-BTC composite fabricated using in-situ technique; C2, C3, C4: CNF/Cu-BTC composite synthesized via ex-situ method using triethylamine, citric acid, and glutaraldehyde, respectively.

3.2. Initial performance comparison of CNF, Cu-BTC, and composites on the curcumin uptake

The initial performance of all samples on the uptake of curcumin is conducted; the results are summarized in Fig. 7. The adsorption capacities of CNF, Cu-BTC, C1, C2, C3, and C4 are found at 40.77 mg/g, 150.7 mg/g, 386.0 mg/g, 688.7 mg/g, 347.4 mg/g, 294.8 mg/g, respectively. The significant difference in the curcumin uptake performance between the single component (CNF and Cu-BTC) and the composites (C1, C2, C3, and C4) shows that the material's interior structure and functional groups are essential in increasing the performance. The role of cellulose as a matrix for the distribution and deposition of Cu-BTC hinders the aggregation of these particular MOF particles, creating more significant numbers of binding sites for curcumin. The mechanism of curcumin adsorption to the CNF/Cu-BTC composites (C1, C2, C3, and C4) is predicted to be driven by the presence of hydroxyl (–OH) and enol groups in curcumin, which are connected to the composite, which also possesses a hefty number of –OH groups and oxygen, coming from TEMPO oxidation; creating hydrogen bonds between the composite and the drug. Theoretically, the presence of TEA, citric acid, and glutaraldehyde as organic linkers provides a more significant number of binding sites (–OH groups and oxygen) in C2, C3, and C4. However, C2 achieves

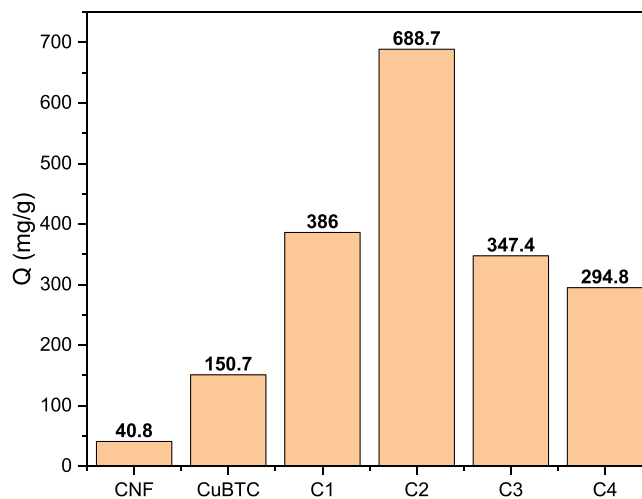


Fig. 7. The curcumin uptake capacity of CNF, Cu-BTC, C1, C2, C3, and C4 (solid loading = 0.1 %, $C_o = 1000$ mg/L, $t = 24$ h, $pH = 7$, $T = 25^\circ\text{C}$).

the highest adsorption capacity in this work compared with the other composites. This might be due to the formation of a three-dimensional matrix promoted by TEA, which increases surface availability [32,40]. Meanwhile, the uptake capacity of C4 is the lowest, which is attributed to the solid aggregation in C4 (as seen in SEM images – Fig. 2). This particle agglomeration significantly lowers the active area for binding, which contributes to the low uptake capabilities (Mahmoodi and Abdi, 2019). The citric acid-crosslinked composite, C3, shows a considerably lower uptake capacity than C1 and C2. Mali et al. (2018) studied that the overall neutral charge owned by citric acid may hinder the adsorption (Mali et al., 2018).

The statistical t-test of the curcumin uptake capacity of all materials, presented in Table 2, is conducted to determine the p-value using a 95 % confidence level. The p-value lower than 0.05 ($p < 0.05$) indicates that

Table 2

The statistical t-test result of CNF, Cu-BTC, C1, C2, C3, and C4.

1st material ^a	2nd material ^a	p-value	
<i>In-situ composite</i> C1	<i>Ex-situ composites</i> C2	1.2×10^{-6}	Significant
	C3	1.9×10^{-2}	Significant
	C4	3.9×10^{-3}	Significant
<i>Ex-situ composites</i> C2	<i>Ex-situ composites</i> C3	2.6×10^{-6}	Significant
	C4	5.2×10^{-5}	Significant
	C4	2.1×10^{-2}	Significant
<i>Ex-situ composite</i> C2	<i>Single component</i> CNF	1.3×10^{-6}	Significant
	Cu-BTC	9.3×10^{-8}	Significant

^a C1: CNF/Cu-BTC composite fabricated using in-situ technique; C2, C3, C4: CNF/Cu-BTC composite synthesized via ex-situ method using triethylamine, citric acid, and glutaraldehyde, respectively.

the comparison between the composite materials is statistically significant. As seen from Table 2, the uptake capacities of ex-situ composites are significantly higher than that of C1, with C2 being the highest. This is likely due to the hefty CH₂ groups in the TEA linker, increasing the

ability of electron transfer between curcumin and the surface of C2. Moreover, a significant difference in the curcumin uptake capacity is also observed when C2 is compared with its single constituting materials (CNF and Cu-BTC). A more elaborate study to compare the performance and behavior of all composites is discussed in the following sections.

3.3. The pH influence on the curcumin uptake of various composites

Fig. 8 shows that the pH condition on the curcumin uptake of various composites does not give any significant changes, indicating that the adsorption behaviors of the composites do not depend on the surface charge. The highest uptake performance of curcumin is monitored at C2, likely due to the higher number of CH₂ groups – originating from TEA compared with other crosslinkers. The CH₂ interaction of composites and curcumin follows the Van Der Waals principle. According to Li et al. (2019), adding TEA to Cu-BTC significantly influences the particles' electron transfer ability and active response, resulting in higher uptake performance than other composites. In addition, the TEA structure consists of nitrogen and methyl groups, which can assist in the attachment of curcumin to C2.

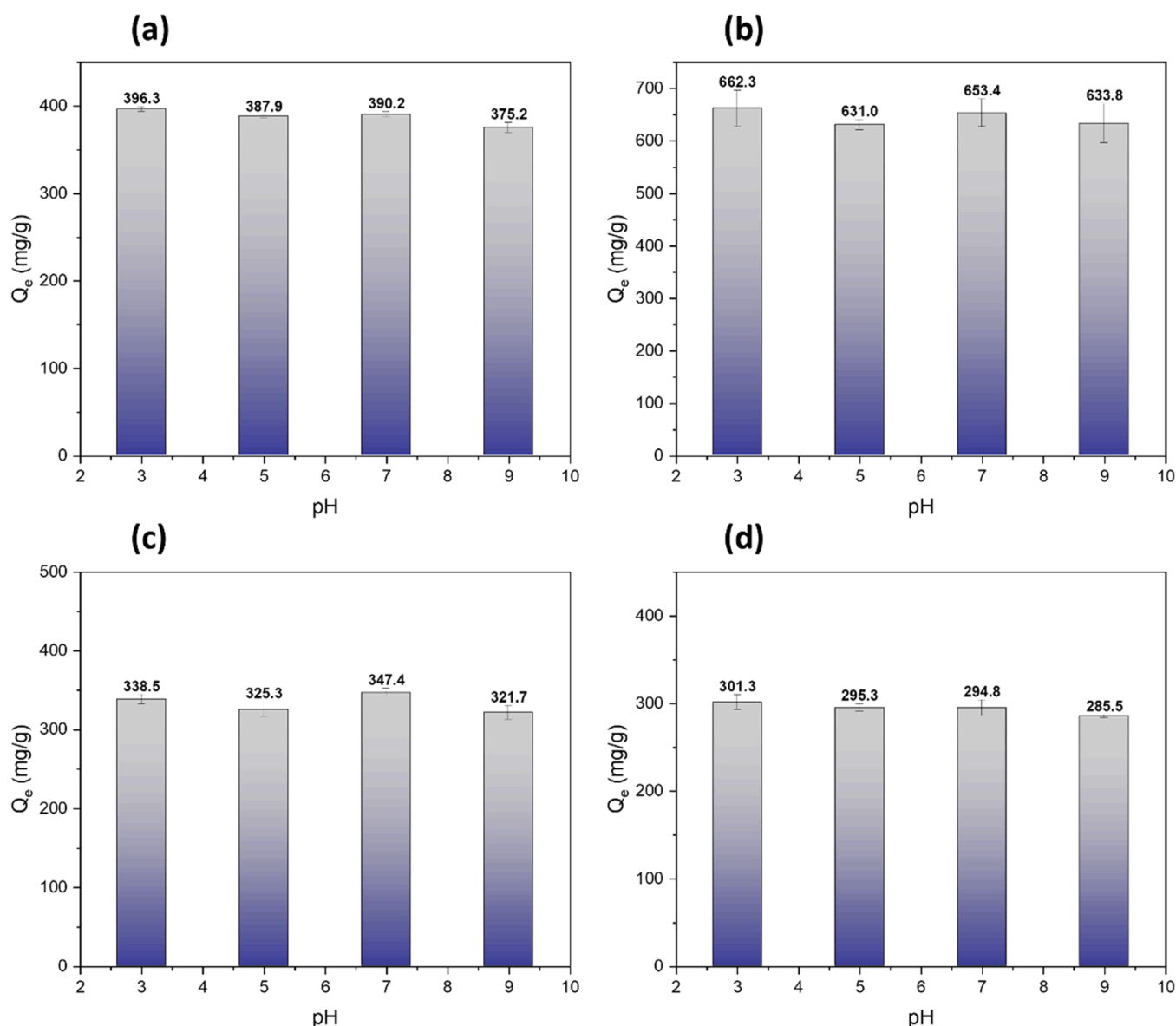


Fig. 8. The influence of pH on the curcumin uptake performance: (a) C1, (b) C2, (c) C3, (d) C4 (composite loading = 0.1 %, $C_o = 1000$ mg/L, $t = 24$ h, and $T = 25^\circ\text{C}$).

3.4. Behavioral studies of curcumin uptake by CNF/Cu-BTC composites

The kinetic profile of various composites can be seen in Figure S2 to study the behavior of the curcumin uptake into various composites, and the fitted parameters are summarized in Table S4. Figure S2 shows a rapid increase in the adsorption of curcumin at the first 100 min and reaches equilibrium at 1440 min for all composites. The loading capacity escalates when the temperature increases from 30°C to 50°C, showing an increase in the diffusion rate of curcumin across all composites. Based on the computed parameters (Table S4), the experimental data show a better fit to PSO than PFO, suggesting the governing mechanism is mainly chemical interaction. However, since the general PFO and PSO equation does not take account of the boundary layer or external resistance, the chemical interaction is not necessarily the rate-limiting step of the adsorption since a good fit does not determine the fundamental nature of the rate-limiting step. Adding half-time (τ) in the equation (to become modified PFO and modified PSO) may improve the accuracy of determining the rate-limiting step as described by (Hu et al., 2022). The changes in good fitting from PSO to PFO across all composites suggest that the adsorption mechanism is closer to physisorption. These findings are further described by the adsorption mechanism of the composites, which is hydrogen bonding between the phenyl group from curcumin and the OH group from Cu-BTC.

Further, the curcumin adsorption to the composites does not change the chemical structure of the composites, which is in line with previous studies (Liang et al., 2022; Munasinghe et al., 2023). The employed MPO model supposedly shows the linear combination of first- and second-order, resulting in various intermediate behaviors between the PFO and PSO models. However, due to the unfitting of the PSO model, the MPO model cannot be calculated further, confirming the non-existence of PSO as the rate-limiting step. The n -value on the calculated PNO model of all composites is obtained at $n = 0.3$, indicating that the order of PNO is near to the first order and confirms the physisorption nature of adsorption. Using the modified PFO model as the best fit, the calculated equilibrium capacity in all composites shows the tendency to escalate with the increase of temperature, implying the endothermic nature of the adsorption. The calculated activation energy is obtained at 29.90 kJ/mol for C1, -12.07 kJ/mol for C2, 0.13 kJ/mol for C3, and 1.44 kJ/mol for C4.

The Webber-Morris model is employed to elaborate further on the adsorption steps in this study. The fitted data are presented in Fig. 9, while the calculated parameters are summarized in Table 3. The migration of curcumin from the bulk solution into the pores of the composites can be described in several steps, which are represented by the dashed line in Fig. 9: (1) The rapid transfer of curcumin from the bulk solution to the surface of the composites; (2) the curcumin slowly

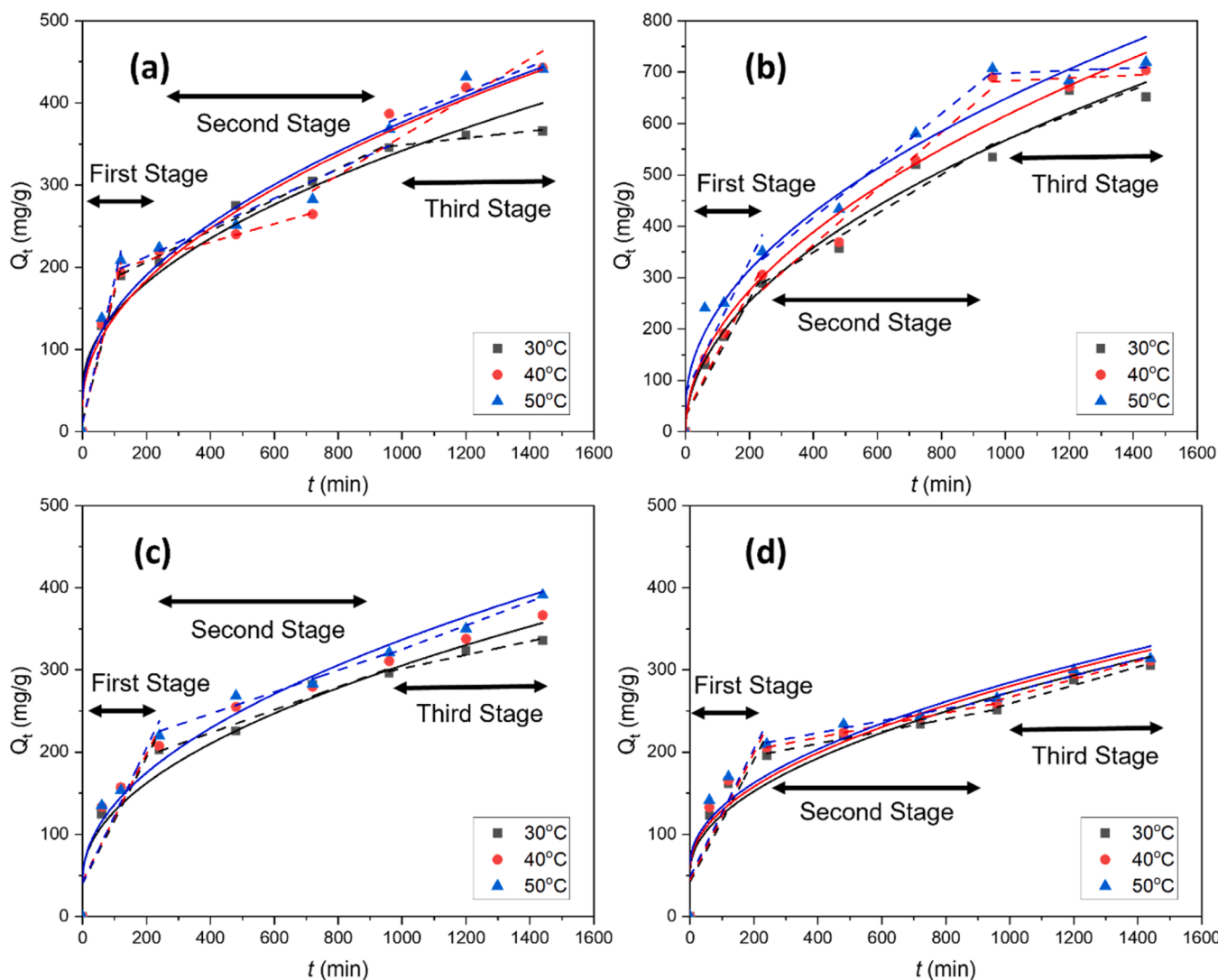


Fig. 9. The Weber-Morris fitted data of various composites: (a) C1, (b) C2, (c) C3, and (d) C4 (solid line represents non-linear Weber-Morris; dashed line represents linear fitting of each stage).

Table 3
The calculated adsorption kinetic parameters by the Weber-Morris model.

Material ^a	Parameters	T (°C)		
		30	40	50
C1	k_{ipd} (mg/g.min ^{0.5})	9.18	10.76	10.63
	k_{ipd1}	1.58	1.62	1.70
	k_{ipd2}	0.18	0.11	0.17
	k_{ipd3}	0.04	0.24	0.15
	C	51.50	32.20	40.19
	R^2	0.94	0.94	0.94
C2	k_{ipd} (mg/g.min ^{0.5})	17.93	19.44	19.04
	k_{ipd1}	1.13	1.19	1.27
	k_{ipd2}	0.37	0.54	0.50
	k_{ipd3}	0.24	0.03	0.02
	C	8.9×10^{-19}	8.9×10^{-23}	45.9
	R^2	0.98	0.97	0.96
C3	k_{ipd} (mg/g.min ^{0.5})	8.19	9.23	9.26
	k_{ipd1}	0.76	0.77	0.82
	k_{ipd2}	0.14	0.13	0.13
	k_{ipd3}	0.08	0.14	0.14
	C	46.13	43.85	43.80
	R^2	0.94	0.95	0.95
C4	k_{ipd} (mg/g.min ^{0.5})	6.88	6.98	6.98
	k_{ipd1}	0.74	0.77	0.77
	k_{ipd2}	0.07	0.07	0.07
	k_{ipd3}	0.11	0.11	0.09
	C	55.05	59.33	63.80
	R^2	0.90	0.89	0.89

^a C1: CNF/Cu-BTC composite fabricated using in-situ technique; C2, C3, C4: CNF/Cu-BTC composite synthesized via ex-situ method using triethylamine, citric acid, and glutaraldehyde, respectively.

diffuses from the boundary layer to the pores of the composites; and (3) the physical binding of curcumin molecules to active sites of the composites via hydrogen bonding. The fitted adsorption constants for each stage (k_{ipd1} , k_{ipd2} , and k_{ipd3}) from Table 3 demonstrate that k_{ipd1} is more remarkable than other parameters, and all composites exhibit a similar pattern. These findings suggest that the rate-determining phase appears to be the diffusion of curcumin molecules from the bulk solution to the surface of composites. It is followed sequentially by the gradual intraparticle diffusion and the chemical binding of curcumin to composites. The results above are supported by Elovich's theory, which states that the adsorption rate dropped exponentially as the amount adsorbed increased. The endothermic nature of the uptake is verified by the calculated parameters of k_{ipd} , which proportionally inclines along with the temperature.

Figure S3 presents the isotherm profile of the curcumin uptake by various composites, and the calculated parameters are outlined in Table S5. The isotherm profiles of all composites reveal the presence of two stages: (1) the first stage at a low concentration of bulk curcumin solution (0–500 mg/L) shows a tendency to monolayer adsorption, and (2) the higher concentration of curcumin exhibits an aptitude to multilayer adsorption. The findings elaborate that curcumin undergoes competitive adsorption (CoA) at low concentrations where the existing curcumin molecules compete to bind onto the surface of composites. Meanwhile, during the increased concentration of curcumin, the stronger affinity between attached curcumin and free curcumin in bulk solution leads to the occurrence of cooperative adsorption (CA), resulting in the expansion of cluster, creating layers on the surface of the composites, which supports the multilayer concept that was previously observed in the N_2 sorption results.

During the first CoA stage, the equilibrium data better fit the Langmuir model than the Freundlich model. These results suggest that curcumin adsorption in this stage follows a monolayer mechanism and happens homogeneously within the surface of composites. However, the opposite occurs during the second stage, where the Freundlich model best fits the equilibrium data, implying the multilayer adsorption in all composites. The increasing value of q_{m-L} in the first stage is observed in

all composites, which signifies their endothermic natures. It is also supported by the enhanced Temkin constant (K_T) and temperature. The Temkin's heat of sorption (E_T) values at the first and second stages are observed below the minimum energy threshold for chemisorption at 20 kJ/mol (Atkins, 1999), implying the physical interaction between adsorbate and adsorbent. Meanwhile, the D-R's mean sorption energy (E_{D-R}) values of all composites in the first stage are found below 8 kJ/mol, indicating the physisorption. In the second stage, all E_{D-R} values are higher than 8 kJ/mol, revealing that the chemical ion exchange mechanism drives the interaction between the first curcumin layer and the free curcumin.

Further investigation for the multilayer adsorption is conducted using the BET model, as the model can describe the nature of the first and upper layers of the adsorption. The thermodynamic behavior will also be discussed using the resulting parameters. The computed thermodynamic properties (Gibbs free energy (ΔG°), enthalpy (ΔH°), and entropy (ΔS°)) are given in Table 4. The negative values of ΔG° in all composites indicate that curcumin's adsorption on composites happens spontaneously and favorably. At T ranging from 30°C to 50°C, ΔG° values consistently demonstrate stability, signifying the enduring affinity of curcumin to composites amid temperature fluctuations. The positive values of ΔH° in C1 and C4 are positive in the first layers, which exhibit a constant endothermic nature. However, C4 experiences thermodynamic instability in the upper layer because it changes to exothermic. Conversely, the ΔH° values are negative in the first layer of C2 and C3 and positive in their upper layers, also referring to the change of thermodynamic behavior during the uptake. The entropy (ΔS°) of all composites shows a decreasing value from the first layer to the upper layer, implying a decrease in randomness on the surface of the composites at different layers.

3.5. The curcumin release performance and kinetic behavior

The curcumin release from various composites is conducted for 96 h

Table 4
The thermodynamic parameters of the curcumin uptake onto C1, C2, C3, and C4.

Material ^a		T (°C)	ΔH° (kJ/mol)	ΔS° (kJ/mol.K)	ΔG° (kJ/mol)
C1	First Layer	30	9.11	0.99	-292.3
		40			-302.2
		50			-312.3
	Upper Layer	30	9.15	0.08	-15.41
		40			-16.22
		50			-17.03
C2	First Layer	30	-165.4	0.43	-297.2
		40			-301.6
		50			-305.9
	Upper Layer	30	5.78	0.07	-16.74
		40			-17.48
		50			-18.23
C3	First Layer	30	-36.42	0.85	-294.4
		40			-302.8
		50			-311.4
	Upper Layer	30	7.34	0.07	-14.81
		40			-15.54
		50			-16.27
C4	First Layer	30	31.06	1.08	-297.4
		40			-308.3
		50			-319.1
	Upper Layer	30	-0.38	0.05	-14.67
		40			-15.14
		50			-15.61

^a C1: CNF/Cu-BTC composite fabricated using in-situ technique; C2, C3, C4: CNF/Cu-BTC composite synthesized via ex-situ method using triethylamine, citric acid, and glutaraldehyde, respectively.

at pH 5.5 and 7.4 to mimic the blood plasma condition. The release data, plotted in Fig. 10, reveals the slow release behavior of all composites between the first minute of release and 600 min, followed by a constant-rate release to achieve maximum cumulative release. This behavior is beneficial because the drug is released in a controlled manner. The likelihood of adverse consequences from an abrupt burst release may likewise be decreased, if not eliminated, by such a gradual release. Additionally, it can potentially have a long-lasting, consistent therapeutic effect.

Fig. 10 illustrates that the release of C1 is 23.20 % at pH = 7.4 and increases to 26.30 % at pH = 5.5. For C2, the release is 36.70 % at pH 7.4 and rises to 39.10 % at pH 5.5. Meanwhile, C3 shows a release of 30.20 % at pH 7.4, increasing to 35.28 % at pH 5.5, and lastly, C4 has a release of 22.10 % at pH 7.4 and decreases to 19.50 % at pH 5.5. The pH responses at acidic conditions for composite material provoke the metal-ligand framework to degrade; hence, it is beneficial to prevent premature curcumin release. Among all composites, the lowest cumulative release happens in C1, the CNF/Cu-BTC composite synthesized via in-situ technique. The lack of linkers in C1 is predicted to be the main reason for this low cumulative release, as linkers generally initiate the degradation of the composites and increase the release capacity.

Meanwhile, the highest release is observed in C2. It can be attributed

to the basic nature of TEA, which is more sensitive to acidic environments and leads to electron exchange. The interaction causes the composite structure to be readily degraded and more prone to release the confined curcumin, resulting in a higher release than the other composites. Unlike TEA, both citric acid and glutaraldehyde are weak acids – in acidic conditions, both components are harder to degrade and, instead, retain their structures (He et al., 2021; Mali et al., 2018; Mikušová and Mikuš, 2021).

To further understand the release mechanism of C1, C2, C3, and C4, several release kinetic models, e.g., Higuchi, Hixson-Crowell, and Korsmeyer-Peppas, are fitted to the data, and the results are presented in Table S6. Among the three models, the Korsmeyer-Peppas model is well-fitted to the release data of all composites with $R^2 > 0.84$, followed by Higuchi – suggesting the slow diffusion rate. According to the literature, the release mechanism of any polymer material generally follows one of two pathways: chemical (solute diffusion, degradation of material) or physical (swelling of polymer) routes (Korsmeyer et al., 1983), and is indicated by the n value (the transport constant or the release exponent) of Korsmeyer-Peppas model. Table S6 shows that the n values in all materials are less than 0.5, indicating the curcumin release via a chemical pathway – where the degradation of the material's structure due to pH sensitivity and subsequent solute diffusion from the matrices

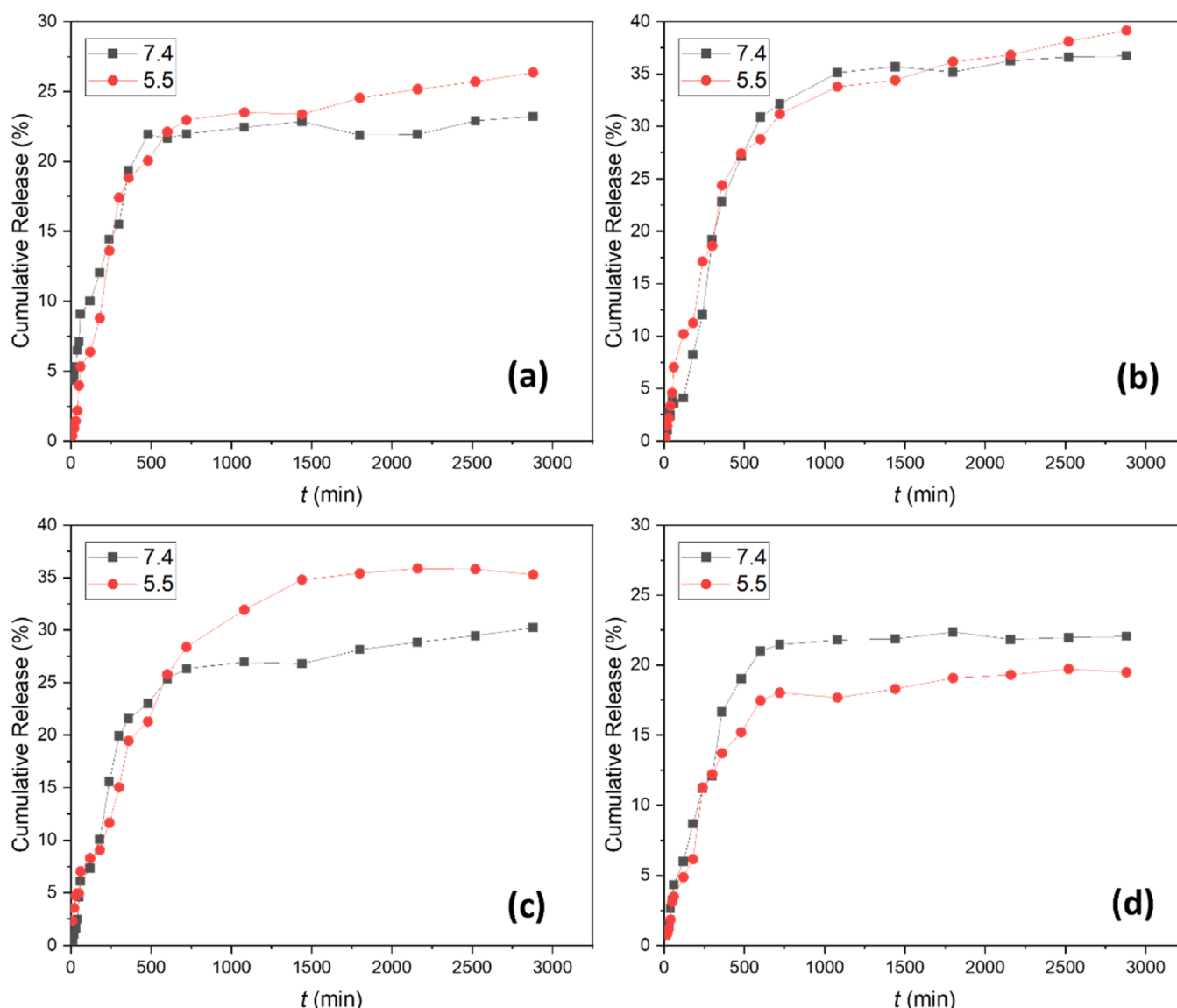


Fig. 10. The curcumin release profile of various composites: (a) C1, (b) C2, (c) C3, and (d) C4 at pH = 5.5 and pH = 7.4.

happens during the release.

The release rate constant of Korsmeyer-Peppas (K_{KP}) shows that a higher K_{KP} value indicates fast release, while a lower K_{KP} value indicates low transport kinetic. The K_{KP} values of C2 – C4 are between the highest (0.034) and the lowest (0.013), implying a sustained release compared to C1. A non-linear trend of Hixson-Crowell is observed in all materials, suggesting that curcumin release is oppositely proportional with a surface area of C1-C4 (Abdelhameed et al., 2017; Ani Jose, 2018; Emam and Mohamed, 2021; Emam and Shaheen, 2022; Wu et al., 2019). Based on the results, it can be concluded that the drug transport mechanism follows (1) the Quasi-Fickian diffusion, (2) the first-order transport, and (3) the non-swellable mechanism.

4. Conclusions

This study compares the curcumin uptake capabilities of CNF/Cu-BTC composites synthesized using in-situ (C1) and ex-situ (C2) methods. The maximum curcumin uptake of C1, C2, C3, and C4 at the respective values of 386.0 mg/g, 688.7 mg/g, 347.4 mg/g, and 294.8 mg/g is significantly higher compared with that of CNF (40.77 mg/g) and Cu-BTC (150.7 mg/g). The enhanced uptake capacity of C1, C2, C3, and C4 can be ascribed to the composite materials' three-dimensional structure, increasing their textural properties. Moreover, the dispersity of Cu-BTC on the surface of CNF creates a more significant number of binding sites for curcumin – heightening the uptake performance. The uptake behavior of curcumin follows the modified PFO model with half-time (τ) with CoA adsorption (monolayer mechanism) at low curcumin concentration and CA adsorption (multilayer aptitude) at high concentrations of curcumin. The interaction for all composites is governed by hydrogen bonding, where the hydroxyl (–OH) and enol groups of curcumin bind the –OH groups and oxygen owned by the composites. The release performance for all composites is slow and controllable. The cumulative release is higher for C2 than the other composites due to C2's crosslinker (TEA) sensitivity to the acidic environment. All composites (C1, C2, C3, and C4) show better performance in the uptake/release of curcumin than the single CNF and Cu-BTC materials, with excellent uptake/release capabilities in C2. Therefore, the valorization of CHW to CNF/Cu-BTC composite will prominently reduce waste and, at the same time, offer a better route for waste circularity, as it may benefit the pharmaceutical and health sectors.

CRedit authorship contribution statement

Michael Giovanni Sugiarto: Investigation. **Suryadi Ismadji:** Resources, Funding acquisition. **Christian Julius Wijaya:** Supervision, Methodology, Data curation. **Maria Yuliana:** Writing – review & editing, Supervision, Resources, Project administration, Methodology, Funding acquisition, Conceptualization. **Puong Lan Tran-Nguyen:** Software, Investigation. **Marvel Guntur Wijanarko:** Writing – original draft, Visualization, Software, Methodology, Investigation, Conceptualization. **Felycia Edi Soetaredjo:** Resources, Funding acquisition. **Sandy Budi Hartono:** Validation. **Wenny Irawaty:** Validation. **Shella Permatasari Santoso:** Validation. **Hidayat Hidayat:** Software, Investigation. **Grandprix Thomryes Marth Kadja:** Software, Investigation.

Declaration of Competing Interest

The authors declare that they have no known competing financial interests or personal relationships that could have appeared to influence the work reported in this paper.

Acknowledgement

The authors thank the Institut Teknologi Bandung and the National Research and Innovation Agency, Indonesia, for providing the facilities for material characterizations. This project was supported by the

Ministry of Education, Culture, Research, and Technology of the Republic of Indonesia through research grant no. 570A/WM01.5/N/2024, 268G/WM01.5/N/2023 and 260C/WM01.5/N/2023.

Appendix A. Supporting information

Supplementary data associated with this article can be found in the online version at doi:10.1016/j.indcrop.2024.120048.

Data availability

Data will be made available on request.

References

- Abdelhameed, R.M., Abdel-Gawad, H., Elshahat, M., Emam, H.E., 2016. Cu-BTC@cotton composite: design and removal of ethion insecticide from water. *RSC Adv.* 6, 42324–42333. <https://doi.org/10.1039/c6ra04719j>.
- Abdelhameed, R.M., Emam, H.E., Rocha, J., Silva, A.M.S., 2017. Cu-BTC metal-organic framework natural fabric composites for fuel purification. *Fuel Process. Technol.* 159, 306–312. <https://doi.org/10.1016/j.fuproc.2017.02.001>.
- Abdelhameed, R.M., El-Deib, H.R., El-Dars, F.M.S.E., Ahmed, H.B., Emam, H.E., 2018. Applicable strategy for removing liquid fuel nitrogenated contaminants using MIL-53-NH2@natural fabric composites. *Ind. Eng. Chem. Res.* 57, 15054–15065. <https://doi.org/10.1021/acs.iecr.8b03936>.
- Abdelhameed, R.M., Alzahrani, E., Shaltout, A.A., Emam, H.E., 2021. Temperature-controlled-release of essential oil via reusable mesoporous composite of microcrystalline cellulose and zeolitic imidazole frameworks. *J. Ind. Eng. Chem.* 94, 134–144. <https://doi.org/10.1016/j.jiec.2020.10.025>.
- Abdelhamid, H.N., Georgouvelas, D., Edlund, U., Mathew, A.P., 2022. CelloZIFPaper: cellulose-ZIF hybrid paper for heavy metal removal and electrochemical sensing. *Chem. Eng. J.* 446. <https://doi.org/10.1016/j.cej.2022.136614>.
- Adeosun, S.O., Ilomuanya, M.O., Gbenedor, O.P., Dada, M.O., Odili, C.C., Adeosun, S.O., Ilomuanya, M.O., Gbenedor, O.P., Dada, M.O., Odili, C.C., 2020. Biomaterials for drug delivery: sources, classification, synthesis, processing, and applications. *Adv. Funct. Mater.* <https://doi.org/10.5772/INTECHOPEN.93368>.
- Ani Jose, P., 2018. RELEASE KINETICS-CONCEPTS AND APPLICATIONS.
- Atkins, P., 1999. *Physical Chemistry*, 6th edition. Oxford University Press, London (ed).
- Chen, Q., Chen, Q.W., Zhuang, C., Tang, P.P., Lin, N., Wei, L.Q., 2017. Controlled release of drug molecules in metal-organic framework material HKUST-1. *Inorg. Chem. Commun.* 79, 78–81. <https://doi.org/10.1016/j.inoche.2017.03.027>.
- Chen, Y., Mu, X., Lester, E., Wu, T., 2018. High efficiency synthesis of HKUST-1 under mild conditions with high BET surface area and CO2 uptake capacity. *Prog. Nat. Sci.: Mater. Int.* 28, 584–589. <https://doi.org/10.1016/j.pnsc.2018.08.002>.
- Dinand, E., Chanzy, H., Vignon, M.R., 1996. Parenchymal cell cellulose from sugar beet pulp: preparation and properties. *Cellulose* 3, 183–188. <https://doi.org/10.1007/BF02228800/METRICS>.
- Diring, S., Furukawa, S., Takashima, Y., Tsuruoka, T., Kitagawa, S., 2010. Controlled multiscale synthesis of porous coordination polymer in nano/micro regimes. *Chem. Mater.* 22, 4531–4538. <https://doi.org/10.1021/cm101778g>.
- Emam, H.E., Abdelhameed, R.M., 2017. In-situ modification of natural fabrics by Cu-BTC MOF for effective release of insect repellent (N,N-diethyl-3-methylbenzamide). *J. Porous Mater.* 24, 1175–1185. <https://doi.org/10.1007/s10934-016-0357-y>.
- Emam, H.E., Mohamed, A.L., 2021. Controllable release of povidone-iodine from networked pectin@carboxymethyl pullulan hydrogel. *Polym. (Basel)* 13. <https://doi.org/10.3390/polym131831118>.
- Emam, H.E., Shaheen, T.I., 2022. Design of a dual pH and temperature responsive hydrogel based on esterified cellulose nanocrystals for potential drug release. *Carbohydr. Polym.* 278. <https://doi.org/10.1016/j.carbpol.2021.118925>.
- Emam, H.E., El-Shahat, M., Taha, M., Abdelhameed, R.M., 2022. Microwave assisted post-synthetic modification of IRMOF-3 and MIL-68-NH2 onto cotton for Fuel purification with computational explanation. *Surf. Interfaces* 30. <https://doi.org/10.1016/j.surfin.2022.101940>.
- Emam, H.E., Ahmed, H.B., El-Shahat, M., Abdel-Gawad, H., Abdelhameed, R.M., 2023. Selective separation of chlorophyll-a using recyclable hybrids based on Zn-MOF@cellulosic fibers. *Sci. Rep.* 13. <https://doi.org/10.1038/s41598-023-42151-9>.
- Feng, L., Wang, K.Y., Powell, J., Zhou, H.C., 2019. Controllable synthesis of metal-organic frameworks and their hierarchical assemblies. *Matter*. <https://doi.org/10.1016/j.matt.2019.08.022>.
- Gao, J., Karp, J.M., Langer, R., Joshi, N., 2023. The future of drug delivery. *Chem. Mater.* <https://doi.org/10.1021/acs.chemmater.2c03003>.
- Gautam, S., Singhal, J., Lee, H.K., Chae, K.H., 2022. Drug delivery of paracetamol by metal-organic frameworks (HKUST-1): improvised synthesis and investigations. *Mater. Today Chem.* 23. <https://doi.org/10.1016/j.mtchem.2021.100647>.
- George, P., Das, R.K., Chowdhury, P., 2019. Facile microwave synthesis of Ca-BDC metal organic framework for adsorption and controlled release of Curcumin. *Microporous Mesoporous Mater.* 281, 161–171. <https://doi.org/10.1016/j.micromeso.2019.02.028>.
- Hao, S., Yuling, L., Yang, J., 2022. Construction of Cu-BTC by carboxylic acid organic ligand and its application in low temperature SCR denitration. *Sci. Total Environ.* 820. <https://doi.org/10.1016/j.scitotenv.2022.152984>.

- He, S., Wu, L., Li, X., Sun, Hongyu, Xiong, T., Liu, J., Huang, C., Xu, H., Sun, Huimin, Chen, W., Gref, R., Zhang, J., 2021. Metal-organic frameworks for advanced drug delivery. *Acta Pharm. Sin. B* 11, 2362–2395. <https://doi.org/10.1016/j.apsb.2021.03.019>.
- Hu, Q., Pang, S., Wang, D., 2022. In-depth insights into mathematical characteristics, selection criteria and common mistakes of adsorption kinetic models: a critical review. *Sep. Purif. Rev.* <https://doi.org/10.1080/15422119.2021.1922444>.
- Huo, Y., Liu, Y., Xia, M., Du, H., Lin, Z., Li, B., Liu, H., 2022. Nanocellulose-based composite materials used in drug delivery systems. *Polymers.* <https://doi.org/10.3390/polym14132648>.
- Isogai, A., Saito, T., Fukuzumi, H., 2011. TEMPO-oxidized cellulose nanofibers. *Nanoscale.* <https://doi.org/10.1039/c0nr00583e>.
- Jeromenok, J., Weber, J., 2013. Restricted access: on the nature of adsorption/desorption hysteresis in amorphous, microporous polymeric materials. *Langmuir* 29, 12982–12989. https://doi.org/10.1021/LA402630S/SUPPL_FILE/LA402630S_SI_001.PDF.
- Kolakovic, R., Peltonen, L., Laukkanen, A., Hirvonen, J., Laaksonen, T., 2012. Nanofibrillar cellulose films for controlled drug delivery. *Eur. J. Pharm. Biopharm.* 82, 308–315. <https://doi.org/10.1016/j.ejpb.2012.06.011>.
- Kolakovic, R., Peltonen, L., Laukkanen, A., Hellman, M., Laaksonen, P., Linder, M.B., Hirvonen, J., Laaksonen, T., 2013. Evaluation of drug interactions with nanofibrillar cellulose. *Eur. J. Pharm. Biopharm.* 85, 1238–1244. <https://doi.org/10.1016/j.ejpb.2013.05.015>.
- Korsmeyer, R.W., Gurny, R., Doelker, E., Buri, P., Peppas, N.A., 1983. Mechanisms of solute release from porous hydrophilic polymers. *Int. J. Pharm.*
- Li, C., Hao, J., Wu, K., 2019. Triethylamine-controlled Cu-BTC frameworks for electrochemical sensing fish freshness. *Anal. Chim. Acta* 1085, 68–74. <https://doi.org/10.1016/j.aca.2019.07.064>.
- Li, Y., Xia, X., Hou, W., Lv, H., Liu, J., Li, X., 2023. How effective are metal nanotherapeutic platforms against bacterial infections? A comprehensive review of literature. *Int. J. Nanomed.* <https://doi.org/10.2147/IJN.S397298>.
- Liang, Y., Yao, Y., Liu, Y., Li, Y., Xu, C., Fu, L., Lin, B., 2022a. Curcumin-loaded HKUST-1@ carboxymethyl starch-based composites with moisture-responsive release properties and synergistic antibacterial effect for perishable fruits. *Int. J. Biol. Macromol.* 214, 181–191. <https://doi.org/10.1016/j.jbiomac.2022.06.022>.
- Liu, R., He, X., Miao, M., Cao, S., Feng, X., 2022. In-situ growth of porous Cu₃(BTC)₂ on cellulose nanofibrils for ultra-low dielectric films with high flexibility. *J. Mater. Sci. Technol.* 112, 202–211. <https://doi.org/10.1016/j.jmst.2021.09.055>.
- Löbmann, K., Wohler, J., Müllertz, A., Wägberg, L., Svagan, A.J., 2017. Cellulose nanopaper and nanofoam for patient-tailored drug delivery. *Adv. Mater. Interfaces* 4. <https://doi.org/10.1002/admi.201600655>.
- Mahmoodi, N.M., Abdi, J., 2019. Metal-organic framework as a platform of the enzyme to prepare novel environmentally friendly nanobio-catalyst for degrading pollutant in water. *J. Ind. Eng. Chem.* 80, 606–613. <https://doi.org/10.1016/j.jiec.2019.08.036>.
- Mali, K.K., Dhawale, S.C., Dias, R.J., Dhane, N.S., Ghorpade, V.S., 2018. Citric acid crosslinked carboxymethyl cellulose-based composite hydrogel films for drug delivery. *Indian J. Pharm. Sci.* 80, 657–667. <https://doi.org/10.4172/PHARMACEUTICAL-SCIENCES.1000405>.
- Mallakpour, S., Nikkhoo, E., Hussain, C.M., 2022. Application of MOF materials as drug delivery systems for cancer therapy and dermal treatment. *Coord. Chem. Rev.* <https://doi.org/10.1016/j.ccr.2021.214262>.
- Mikušová, V., Mikuš, P., 2021. Advances in chitosan-based nanoparticles for drug delivery. *Int. J. Mol. Sci.* 22. <https://doi.org/10.3390/IJMS22179652>.
- Munasinghe, V.K., Manawadu, D., de Silva, R.M., de Silva, K.M.N., 2023a. Impact of active sites on encapsulation of curcumin in metal organic frameworks. *Mater. Res Express* 10. <https://doi.org/10.1088/2053-1591/acc445>.
- Peedikakkal, A.M.P., Aljundi, I.H., 2020. Mixed-metal Cu-BTC metal-organic frameworks as a strong adsorbent for molecular hydrogen at low temperatures. *ACS Omega* 5, 28493–28499. <https://doi.org/10.1021/acsomega.0c02810>.
- Sangian, H.F., Widjaja, A., 2018. The effect of alkaline concentration on coconut husk crystallinity and the yield of sugars released. *IOP Conference Series: Materials Science and Engineering.* Institute of Physics Publishing. <https://doi.org/10.1088/1757-899X/306/1/012046>.
- Sarkar, G., Orasugh, J.T., Saha, N.R., Roy, I., Bhattacharyya, A., Chattopadhyay, A.K., Rana, D., Chattopadhyay, D., 2017. Cellulose nanofibrils/chitosan based transdermal drug delivery vehicle for controlled release of ketorolac tromethamine. *N. J. Chem.* 41, 15312–15319. <https://doi.org/10.1039/c7nj02539d>.
- Setyaningsih, D., Uju, Muna, N., Isroi, Suryawan, N.B., Nurfauzi, A.A., 2018. Cellulose nanofiber isolation from palm oil Empty Fruit Bunches (EFB) through strong acid hydrolysis. In: *IOP Conference Series: Earth and Environmental Science.* Institute of Physics Publishing. <https://doi.org/10.1088/1755-1315/141/1/012027>.
- Shih, Y.F., Kotharangannagari, V.K., Tsou, T.C., 2020. Development of eco-friendly modified cellulose nanofiber reinforced polystyrene nanocomposites: thermal, mechanical, and optical properties. *J. Polym. Res.* 27. <https://doi.org/10.1007/s10965-020-02156-8>.
- da Silva Pinto, M., Sierra-Avila, C.A., Hinestroza, J.P., 2012. In situ synthesis of a Cu-BTC metal-organic framework (MOF 199) onto cellulose fibrous substrates: Cotton. *Cellulose* 19, 1771–1779. <https://doi.org/10.1007/s10570-012-9752-y>.
- Svagan, A.J., Müllertz, A., Löbmann, K., 2017. Floating solid cellulose nanofiber nanofoams for sustained release of the poorly soluble model drug furosemide. *J. Pharm. Pharmacol.* 69, 1477–1484. <https://doi.org/10.1111/jphp.12793>.
- Thommes, M., Kaneko, K., Neimark, A.V., Olivier, J.P., Rodriguez-Reinos, F., Rouquerol, J., Sing, K.S.W., 2015. Physisorption of gases, with special reference to the evaluation of surface area and pore size distribution (IUPAC Technical Report). *Pure Appl. Chem.* 87, 1051–1069. <https://doi.org/10.1515/pac-2014-1117>.
- Tu, K., Ding, Y., Keplinger, T., 2022. Review on design strategies and applications of metal-organic framework-cellulose composites. *Carbohydr. Polym.* 291. <https://doi.org/10.1016/j.carbpol.2022.119539>.
- Umemura, A., Diring, S., Furukawa, S., Uehara, H., Tsuruoka, T., Kitagawa, S., 2011. Morphology design of porous coordination polymer crystals by coordination modulation. *J. Am. Chem. Soc.* 133, 15506–15513. <https://doi.org/10.1021/ja204233q>.
- Weber, J., Du, N., Guiver, M.D., 2011. Influence of intermolecular interactions on the observable porosity in intrinsically microporous polymers. *Macromolecules* 44, 1763–1767. https://doi.org/10.1021/MA101447H/SUPPL_FILE/MA101447H_SI_001.PDF.
- Wijanarko, M.G., Widagdo, A.J., Ismadji, M.S., Kusuma, K., Yuliana, M., Ismadji, S., Hartono, S.B., Lie, J., Shu, H., Abdullah, H., Kadja, G.T.M., Wijaya, C.J., Soetaredjo, F.E., 2023. Utilization of APTES-functionalized coconut waste-based cellulose microfibrer/zeolitic-imidazolate framework-8 composite for curcumin delivery. *Mater. Today Sustain.* 21. <https://doi.org/10.1016/j.mtsust.2023.100332>.
- Wu, I.Y., Bala, S., Skalko-Basnet, N., di Cagno, M.P., 2019. Interpreting non-linear drug diffusion data: utilizing Korsmeyer-Peppas model to study drug release from liposomes. *Eur. J. Pharm. Sci.* 138. <https://doi.org/10.1016/j.ejps.2019.105026>.
- Yurdakal, S., Garlisi, C., Özcan, L., Bellardita, M., Palmisano, G., 2019. (Photo)catalyst characterization techniques: Adsorption isotherms and BET, SEM, FTIR, UV-Vis, photoluminescence, and electrochemical characterizations, in: *Heterogeneous Photocatalysis: Relationships with Heterogeneous Catalysis and Perspectives.* Elsevier, pp. 87–152. <https://doi.org/10.1016/B978-0-444-64015-4.00004-3>.
- Zhang, W., Pinna, N., 2024. Metal organic frameworks synthesis: the versatility of triethylamine. *Chem. - A Eur. J.* 30. <https://doi.org/10.1002/chem.202304256>.
- Zhang, X.F., Wang, Z., Ding, M., Feng, Y., Yao, J., 2021. Advances in cellulose-metal organic framework composites: preparation and applications. *J. Mater. Chem. A Mater.* <https://doi.org/10.1039/d1ta06468a>.
- Zhao, J., Liu, X., Wu, Y., Li, D.S., Zhang, Q., 2019. Surfactants as promising media in the field of metal-organic frameworks. *Coord. Chem. Rev.* <https://doi.org/10.1016/j.ccr.2019.04.002>.
- Zhu, C., Monti, S., Mathew, A.P., 2020. Evaluation of nanocellulose interaction with water pollutants using nanocellulose colloidal probes and molecular dynamic simulations. *Carbohydr. Polym.* 229. <https://doi.org/10.1016/j.carbpol.2019.115510>.